

MULTI-WAVELENGTH LENS RECONSTRUCTION OF A PLANCK & *HERSCHEL*-DETECTED  
STARBURSTING GALAXYNICHOLAS TIMMONS<sup>1</sup>, ASANTHA COORAY<sup>1</sup>, DOMINIK A. RIECHERS<sup>2</sup>, HOOSHANG NAYYERI<sup>1</sup>, HAI FU<sup>3</sup>, ERIC JULLO<sup>4</sup>,  
MICHAEL D. GLADDERS<sup>5</sup>, MAARTEN BAES<sup>6</sup>, R. SHANE BUSSMANN<sup>2</sup>, JAE CALANOG<sup>7</sup>, DAVID L. CLEMENTS<sup>8</sup>, ELISABETE DA  
CUNHA<sup>9</sup>, SIMON DYE<sup>10</sup>, STEPHEN A. EALES<sup>11</sup>, CRISTINA FURLANETTO<sup>10,12</sup>, JOAQUIN GONZALEZ-NUENO<sup>13</sup>, JOSHUA  
GREENSLADE<sup>8</sup>, MARK GURWELL<sup>14</sup>, MICHAŁ J. MICHAŁOWSKI<sup>15</sup>, IVÁN OTEO<sup>15,16</sup>, ISMAEL PÉREZ-FOURNON<sup>17,18</sup>, DOUGLAS  
SCOTT<sup>19</sup>, ELISABETTA VALIANTE<sup>11</sup><sup>1</sup>Department of Physics and Astronomy, University of California, Irvine, CA 92697<sup>2</sup>Department of Astronomy, Cornell University, Ithaca, NY 14853, USA<sup>3</sup>Department of Physics & Astronomy, University of Iowa, Iowa City, IA 52242<sup>4</sup>Aix-Marseille Université, CNRS, LAM (Laboratoire d'Astrophysique de Marseille) UMR 7326, 38 rue Joliot-Curie, 13388 Marseille  
Cedex, France<sup>5</sup>The Department of Astronomy and Astrophysics, and the Kavli Institute for Cosmological Physics, The University of Chicago, 5640  
South Ellis Avenue, Chicago, IL 60637, USA<sup>6</sup>Sterrenkundig Observatorium, Universiteit Gent, Krijgslaan 281S9, 9000 Gent, Belgium<sup>7</sup>Department of Physical Sciences, San Diego Miramar College, San Diego CA, 92126<sup>8</sup>Physics Department, Blackett Lab, Imperial College, Prince Consort Road, London SW7 2AZ, UK<sup>9</sup>Centre for Astrophysics and Supercomputing, Swinburne University of Technology, Hawthorn, Victoria 3122, Australia<sup>10</sup>School of Physics and Astronomy, The University of Nottingham, University Park, Nottingham, NG7 2RD, UK<sup>11</sup>School of Physics and Astronomy, Cardiff University, Queens Buildings, The Parade, Cardiff CF24 3AA, UK<sup>12</sup>CAPE Foundation, Ministry of Education of Brazil, Brasília/DF, 70040-020, Brazil<sup>13</sup>Departamento de Física, Universidad de Oviedo, C. Calvo Sotelo s/n, 33007 Oviedo, Spain<sup>14</sup>Harvard-Smithsonian Center for Astrophysics, 60 Garden Street, Cambridge, MA 02138<sup>15</sup>Institute for Astronomy, Royal Observatory, Blackford Hill, Edinburgh, EH9 3HJ, United Kingdom<sup>16</sup>European Southern Observatory, Karl-Schwarzschild-Str. 2, 85748 Garching, Germany<sup>17</sup>Instituto de Astrofísica de Canarias (IAC), E-38200 La Laguna, Tenerife, Spain<sup>18</sup>Departamento de Astrofísica, Universidad de La Laguna, E-38206, La Laguna, Tenerife, Spain and<sup>19</sup>Department of Physics & Astronomy, University of British Columbia, 6224 Agricultural Road, Vancouver, BC V6T 1Z1, Canada

Draft version December 20, 2018

## ABSTRACT

We present a reconstruction of a *Herschel* and Planck detected gravitationally-lensed dusty star-forming galaxy (DSFG) at  $z = 1.68$  using *Hubble*, Sub-millimeter Array (SMA), and Keck observations. The background sub-millimeter galaxy (SMG) is strongly lensed by a foreground galaxy cluster at  $z=0.997$  and appears as an arc of length  $\sim 15''$  in the optical images. The continuum dust emission, as seen by SMA, is limited to a single knot within this arc. We present a lens model with source plane reconstructions at several wavelengths to show the difference in magnifications between the stars and the dust and highlight the importance of a multi-wavelength lens models for studies involving lensed DSFGs. We estimate the physical properties of the galaxy by fitting the flux densities to model SEDs leading to a magnification-corrected star-formation rate of  $390 \pm 60 \text{ M}_\odot \text{ yr}^{-1}$  and a stellar mass of  $1.1 \pm 0.4 \times 10^{11} \text{ M}_\odot$ . These values are consistent with high-redshift massive galaxies that have formed most of their stars already. Using the CO  $J = 2 \rightarrow 1$  line intensity we calculate the CO-H<sub>2</sub> conversion factor to be  $1.02 \pm 0.13 \text{ M}_\odot (\text{K km s}^{-1} \text{ pc}^2)^{-1}$ , consistent with the value of  $\sim 0.8$  that is typically used to estimate the molecular gas masses of ultra-luminous galaxies. The estimated gas-to-baryon fraction, molecular gas surface density, and SFR surface density have values of  $0.44 \pm 0.14$ ,  $320 \pm 130 \text{ M}_\odot \text{ pc}^{-2}$ , and  $\sim 33 \pm 14 \text{ M}_\odot \text{ yr}^{-1} \text{ kpc}^{-2}$ , respectively. The ratio of star-formation-rate surface density to molecular gas surface density is higher than that of other measured SMGs and local ULIRGs suggesting a rapid gas consumption time for this galaxy compared to other DSFGs.

*Subject headings:* cosmology: observations — submillimeter: galaxies — infrared: galaxies — galaxies: evolution

## 1. INTRODUCTION

In recent years, large area far-infrared and sub-millimeter surveys, for example, the *Herschel*-Astrophysical TeraHertz Large Area Survey (H-ATLAS) (Eales et al. 2010), have allowed the efficient selection of gravitationally lensed high- $z$  dusty star-forming galaxies (DSFGs) (e.g., Negrello et al. 2007, 2010; González-Nuevo et al. 2012; Wardlow et al. 2013; Bussmann et al. 2013). These DSFGs (see Casey et al. 2014 for a recent review) have star formation rates (SFRs) of  $\sim 10^2 - 10^3 \text{ M}_\odot \text{ yr}^{-1}$ , with typical stellar mass

of  $\sim 10^{11} - 10^{12} \text{ M}_\odot$ , and are generally found during the peak epoch of galaxy formation and evolution at  $z \sim 1 - 4$ . Existing studies (e.g., Ivison et al. 2000; Genzel et al. 2010) show that the rapid star formation is happening in compact regions, giving rise to very high star-formation rate surface densities. Such rapid star-formation has a short lifetime ( $< 0.1 \text{ Gyr}$ ) and is rare in the local Universe (Tacconi et al. 2010a). DSFGs contribute significantly to the cosmic star-formation in the early universe (e.g., Le Floc'h et al. 2005; Gruppioni et al. 2013) and are likely an early stage of today's massive elliptical galaxies (e.g., Lilly et al.

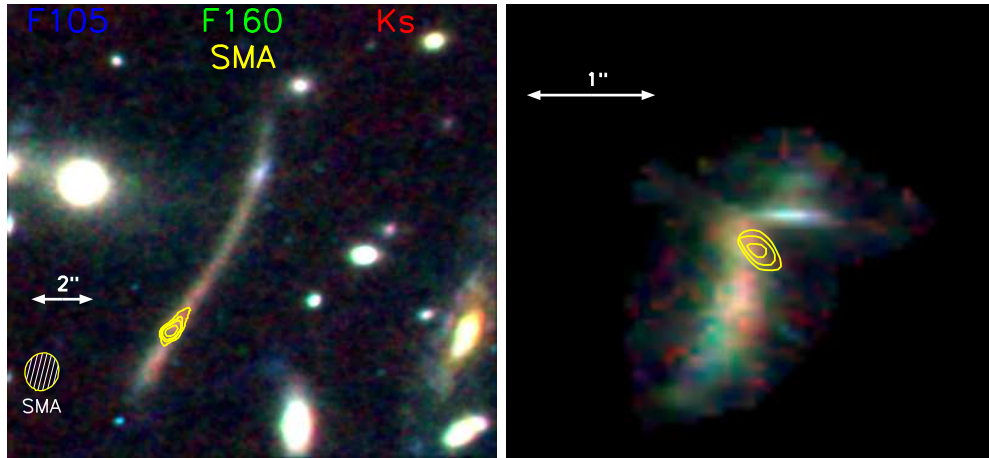


**Figure 1.** *Left:* Three color image of HATLAS J132427+284452 using *Hubble*/WFC3 F105W (blue) and F160W (green), and Keck NIRC2  $K_s$  (red) bands with Submillimeter Array (SMA) 870  $\mu\text{m}$  band emission contours are overlaid. The SMA contours start at  $\sim 5$  mJy and increase by  $\sim 1$  mJy per contour. The dust emission, and thus the *Herschel* and primary Planck source, associated with the DSFG is concentrated in the area of the yellow contours while the optical emission extends over an arc of  $\sim 15''$ . For reference, we show the SMA beam in the bottom left. *Right:* Three color source plane reconstruction with SMA source plane contours overlaid with the same contouring steps as left (see Section 4 for the lens reconstruction). The lens reconstruction clearly shows that the lensed source is composed of at least two sources that are likely undergoing a galaxy merger. The spatial resolution of the reconstruction is  $\sim 0.06''/\text{pixel}$  or  $\sim 0.5$  kpc/pixel.

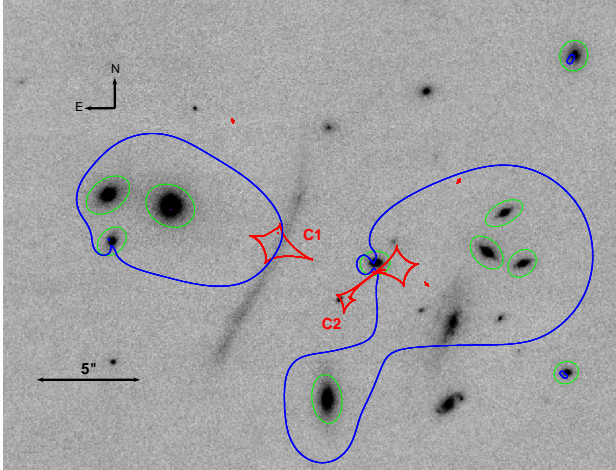


**Figure 2.** Keck/NIRC2  $K_s$ -band image with the critical and caustic (C1 and C2) lines over-plotted in blue and red, respectively. Circled in green are the foreground lens galaxies used in constructing the lens model. In addition to individual galaxies the lensing reconstruction requires extended potential associated with the two galaxy groups/clusters to the east and west of the lensing arc. The cluster component to the east of the lensing arc has an average velocity dispersion of  $\sim 250$  km s $^{-1}$  while the west cluster component has an average velocity dispersion of  $\sim 230$  km s $^{-1}$ .

1999; Swinbank et al. 2006; Lapi et al. 2011; Fu et al. 2013). DSFGs are usually faint at rest-frame optical wavelengths due to dust obscuration, but are bright in the rest-frame far-IR, making sub-mm surveys the perfect tool to study DSFGs (Negrello et al. 2010).

While wide area surveys with *Herschel* and ground-based instruments have increased the sample sizes of DSFGs at sub-mm wavelengths, due to limitations associated with existing instruments in sensitivity and spatial resolution, our ability to conduct detailed investigations on the physical properties of DSFGs has been severely hampered. Thankfully, strong gravitational lensing can be used to overcome these limitations. The flux amplification as a result of gravitational lensing allows for the detection of otherwise intrinsically fainter dust obscured

galaxies and the associated spatial enhancement allows spatially resolved imaging observations with existing facilities (e.g., Fu et al. 2012; Messias et al. 2014).

HATLAS J132427.0+284452 (hereafter HATLAS J132427) peaks at 350  $\mu\text{m}$  with a flux density of  $\sim 380 \pm 8$  mJy (from *Herschel* Spectral and Photometric Imaging Receiver (SPIRE)). It is also identified in the all-sky maps from Planck (Planck Collaboration et al. 2011) as PLCKERC857 G047.32+82.53 ( $1.3 \pm 0.15$  Jy) at 857 GHz (350  $\mu\text{m}$ ) in the Planck Early Release Compact Source Catalog (ERCSC; Planck Collaboration et al. 2011). Although the Planck detected flux density is  $\sim 4\times$  larger than *Herschel*/SPIRE measurement in HATLAS, the difference can be explained as due to the large 3-5 arcmin beam of Planck measurements which may cause blending in an over-dense field. Such a difference is also present in a previous Planck-detected HATLAS J114637.9-001132 (Fu et al. 2012) is detected by Planck with a flux density of  $S_{350} = 2.1 \pm 0.8$  Jy but in *Herschel* the flux density is measured to be  $S_{350} = 378 \pm 28$  mJy corresponding to a  $\sim 5\times$  larger Planck flux density much like HATLAS J132427. Despite the Planck flux being uncertain the detection is validated through other observations and confirms Planck's ability to detect the brightest lensed DSFGs (see Canameras et al. 2015).

In this paper we present new HST, SCUBA2 and Keck observations of HATLAS J132427 along with previous multi-wavelength observations to create a complete profile of this Planck and *Herschel*-detected DSFG. In Section 2 we describe the observations and data reduction procedures. In Section 3 we describe previous and archival observations used in the analysis. In Section 4 we use high resolution imaging to construct a lens model and calculate the magnification factors. In Section 5 we model the spectral energy distribution (SED) and derive physical properties from the fit. In Section 6 we discuss the derived properties of HATLAS J132427 and compare them to other SMGs and DSFGs. We conclude with a summary in Section 7. Throughout we make use of the

**Table 1**  
Observed Properties

Parameter	Value
R.A., DEC	13:24:27.206 +28:44:49.40
$z_{\text{source}}$	$1.676 \pm 0.001$
$z_{\text{lens}}$	$0.997 \pm 0.017$

standard flat- $\Lambda$ CDM cosmological model with  $H_0 = 70$  km s $^{-1}$  Mpc $^{-1}$  and  $\Omega_\Lambda = 0.73$ .

## 2. OBSERVATIONS

Early observations of HATLAS J132427 are presented in George et al. (2013). It remains the only galaxy to date for which the redshift was obtained by far-infrared spectroscopy with the detection of the [CII]/158  $\mu$ m line. Here we present new Keck, SCUBA2, *Hubble*/WFC3 imaging data and *Hubble*/WFC3 grism observations. Figure 1 shows a three color image of the source using HST (F105W and F160W bands) and Keck (Ks band) imaging along with SMA contours overlaid to show the spatial variations of the source at different wavelengths. Figure 2 shows Keck NIRC2 Ks-band imaging with the critical and caustic lines used in the lens model.

### 2.1. Keck/NIRC2

We obtained a 1680 second exposure in H band with an airmass of 1.02 and a 3840 second exposure in K $_s$  band with an airmass of 1.36 (PI: Cooray) on 4 February 2012 with the KeckII/NIRC2 instrument aided with the laser guide-star adaptive optics system (LGSAO; Wizinowich et al. 2006). The imaging observations made use of a pixel scale at 0.04'' pixel $^{-1}$  for both filters. Custom IDL scripts were used to reduce the data following the procedures in Fu et al. (2012, 2013) which includes a dark subtraction, bad pixel masking, background subtraction as well as flat-fielding. The K $_s$ -band image was flux calibrated using UKIDSS (Lawrence et al. 2007) K-band photometry. The H-band image was flux calibrated using a common set of bright stars detected in NIRC2 image and in the *Hubble*/WFC3 F160W band image.

### 2.2. Hubble/WFC3

*Hubble*/WFC3 observations of HATLAS J132427 were completed with three orbits under GO program 13399 in Cycle 21 (PI: Cooray). We obtained a total of ten exposures including two direct images (F105W and F160W) and eight grism observations. The F105W observation had a total exposure time of 453 seconds while the F160W observation had a total exposure time of 353 seconds. Six of the grism observations were taken with the G102 (800 nm - 1150 nm) grism for a total exposure time of 5218 seconds. The remaining two grism observations were taken with the G141 (1075 nm - 1700 nm) grism for a total exposure time of 2406 seconds.

We made use of the calibrated HST imaging and grism data from the CALWF3 reduction pipeline, as provided

by the Space Telescope Science Institute<sup>1</sup>. The spectra for individual objects in the image were extracted with the aXe software package (Kümmel et al. 2009). The data products include the two-dimensional combined grism stamp for each object as well as flux-calibrated one-dimensional spectra, contamination estimates, and error estimates. Similar analysis and reduction steps for the other target, (HATLASJ1429-0028) in GO program 13399 in Cycle 21 are described in Timmons et al. (2015).

The top portion of Figure 3 shows the direct imaging for the F105W and F160W filters aligned so that the dispersion direction of the grism is horizontal. Figure 3 also shows the two-dimensional stamps for the two grism filters. The bottom portion of Figure 3 shows the extracted one-dimensional spectra for each grism filter with a close up view of the two-dimensional continuum shown as an inset. The 2D stamp and the 1D spectra come from the bright northern clump as can be seen in Figure 3. Only the northern clump had a detectable continuum that was not overly contaminated by other spectra in the field. This clump has been circled in blue in the F105W and F160W images in Figure 3. The expected emission lines at  $z = 1.68$  are shown in the 1D spectra of Figure 3 and it is clear there is no significant line detection in either of the grism spectra, and so we cannot conduct line ratio diagnostics on HATLAS J132427. This is due to the low surface brightness of the galaxy compared to the source detected in Timmons et al. (2015) which involved bright multiply-imaged star-forming knots. Unfortunately, due to the overlapping grism spectra from nearby galaxies, we cannot integrate longer to improve the signal-to-noise of the spectrum from our target. This was a challenging observation when proposed in Cycle 21 and our data analysis proves this was indeed the case.

### 2.3. SCUBA2

This source, and the field around it, was observed by the SCUBA2 bolometer array camera on the JCMT (Holland et al. 2013). These observations were part of a broader program following up sources in the H-ATLAS survey (M13AU12, PI D.L. Clements). The observations of the field around HATLAS J132427 were made on 2013 April 8th and 12th using the standard pseudo-circular DAISY observing sequence for small and compact sources. This provides maps of a circular region of roughly 350 arcseconds in radius around the target position. The integration time in this field is a function of position, with the central regions receiving greater integration time than the outer regions. Five separate DAISY maps of HATLAS J132427 were made, three on April 8th, two on April 12th. The conditions for these observations were rated grade 3, indicating  $\tau_{225\text{GHz}}$  0.08 to 0.12. These conditions are adequate for 850  $\mu$ m observations but not for good 450  $\mu$ m photometry.

The data were reduced in the standard manner using the SMURF software provided by the observatory. The SMURF iterative mapmaker *makemap* produced individual maps for each of the five subintegrations using the reduction recipe optimized for blank fields with corrections for atmospheric opacity. The five resulting maps were then combined using the mosaic tool to produce a final image which was then match filtered to optimize

<sup>1</sup> [www.stsci.edu/hst/wfc3/pipeline/wfc3-pipeline](http://www.stsci.edu/hst/wfc3/pipeline/wfc3-pipeline)



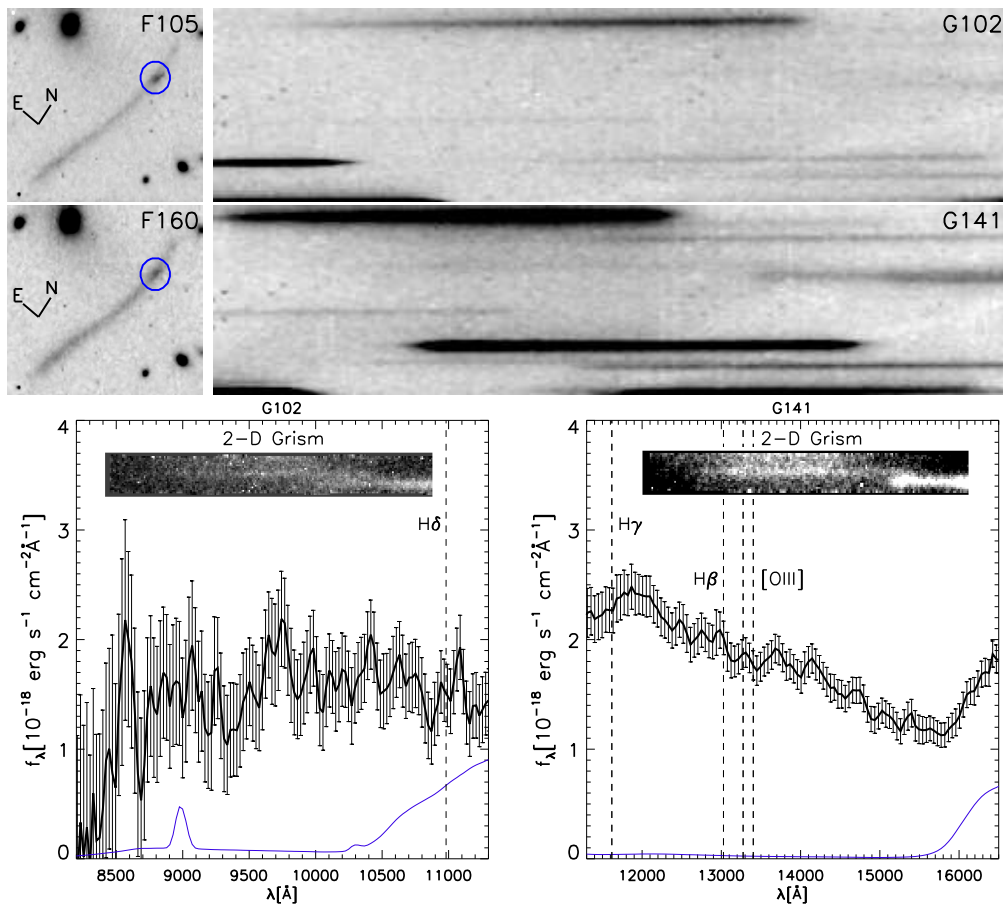


**Figure 3.** *Top Left:* The direct image in each of the WFC3 imaging filters oriented so that the dispersion direction of the grism is horizontal. *Top Right:* The two-dimensional grism images of HATLAS J132427. The top panel shows G102 and F105W images while the middle panel shows G141 and F160W images. *Bottom:* The extracted 1D spectra from the G102 and G141 slitless spectra. The blue line is the estimated contamination coming from other spectra in the field. The 2D grism stamps are inlayed with vertical lines corresponding to useful emission lines over-plotted. Despite the presence of continuum emission no emission lines were detected. Due to contamination from other spectra in the field only the bright northern clump which has been circled in blue had an extractable continuum. It was not possible to extract a 1D spectrum from the southern clump associated with the radio detection.

the S/N of unresolved sources. The final image was then trimmed to produce a 350 arcsecond radius field. The final map has a total integration time of 1850s at its centre, where HATLAS J132427 is located, falling to 450s at the edges. HATLAS J132427 is detected at the centre of the final images with an 850  $\mu\text{m}$  S/N ratio of  $\sim 30$  and a flux of  $43 \pm 1.2$  mJy. It is interesting to note that five other 850  $\mu\text{m}$  sources are detected at  $> 4\sigma$  in the final map, suggesting the presence of a moderate over-density of submm sources around HATLAS J132427.

### 3. PREVIOUS AND ARCHIVAL OBSERVATIONS

HATLAS J132427 was first reported as a candidate strongly lensed giant arc at optical wavelengths in Gladders et al. (2003) and its discovery and follow-up as a bright source in Herschel data is discussed in George et al. (2013). The following is a summary of previous or archival observations that were used for the present analysis. The flux densities are shown in Table 2.

*Herschel* Photoconductor Array Camera and Spectrometer (PACS) (Poglitsch et al. 2010) data at 100  $\mu\text{m}$  and 160  $\mu\text{m}$  were collected as a part of the OT1 program (OT\_RIVISON\_1). The total integration time of 360 seconds reaching  $\sigma \sim 10$  mJy for 100  $\mu\text{m}$  and  $\sigma \sim 12$  mJy for

160  $\mu\text{m}$ . *Herschel*/SPIRE Fourier Transform Spectrometer (FTS) (Griffin et al. 2010) observations were completed on 2 August 2012. The wavelength coverage was  $\lambda_{\text{obs}} = 194 - 671$   $\mu\text{m}$  and the total observing time was 3.8 h. The data resulted in the discovery of the bright [CII]/158  $\mu\text{m}$  emission line with a peak flux density of  $\sim 0.8$  Jy, allowing the redshift of  $z = 1.68$  to be measured directly, for the first time, from far-infrared spectroscopy. While the PACS data are used for the SED analysis the FTS spectrum is not. It is shown in Figure 6 but is not used in the SED analysis due to contamination from the emission line. A detailed re-analysis of the FTS spectrum to search for a broad component of [CII], in comparison to narrow component discussed in George et al. (2013), will be presented in a future publication.

As a part of program 2011B-S044, 870  $\mu\text{m}$  imaging data were taken with the Submillimeter Array (SMA) (PI: Bussmann). The total integration time of 9.7 h was taken in the compact, extended, and very extended array configurations, with baselines of 20-400 m. 1924-292, a blazar, was utilized as a bandpass calibrator and Titan was used for the flux calibration (Bussmann et al. 2013). The SMA continuum is shown in Figure 1 and is used in the lensing model.

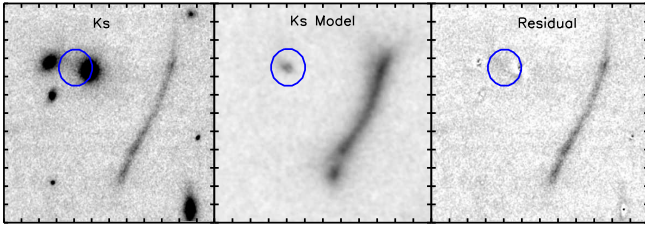


**Figure 4.** *Left:* The Keck/NIRC2  $K_s$ -band image. *Middle:* The  $K_s$ -band model reconstruction in the image plane. *Right:* The  $K_s$ -band image with the foreground galaxies removed using GALFIT. The position of the expected counter-image under the lensing model is circled in blue on each image.

The CO  $J=2 \rightarrow 1$  line ( $\nu_{\text{rest}} = 230.538$  GHz,  $\nu_{\text{obs}} = 86.0$  GHz at  $z=1.68$ ) was detected by the Combined Array for Research in Millimeter-wave Astronomy (CARMA) (PI: Riechers). The observations were conducted on 23 November 2012 using the D configuration (11-146 m baselines). The total on-source time was 2.3 h while two blazars 1310+323 and 0927+390 were used to derive the bandpass shape and for complex gain calibration.

The Canada-Hawaii-France Telescope (CFHT) was used to image HATLAS J132427 in both the  $z$  (925 nm) and  $r$  (640 nm) bands (PI: Yee). The integration times for the  $r$  and  $z$  bands were 900 second and 600 second respectively and the observations were carried out on 5 July 1999 (Gladders et al. 2003). These observations were used to measure  $z=0.9$  for the foreground cluster.

The Institut de Radioastronomie Millimetrique Plateau de Bure Interferometer (IRAM PdBI) was used to obtain 1.1 h of on-source time during November 2012 using six 15 m antennas with the D configuration. The frequency was set to 129.028 GHz. The flux density measurement is used in the SED analysis.

HATLAS J132427 is detected by the Wide Field Infrared Survey Explorer (WISE) in four bands ranging from  $3.35 \rightarrow 22.09$   $\mu\text{m}$  all used in the SED analysis.

#### 4. LENS MODEL

We make use of the program LENSTOOL (Kneib et al. 1996; Jullo et al. 2007) to reconstruct the lensed galaxy and to derive the magnification factors of HATLAS J132427. Using the HST F160W high resolution imaging data, the gravitational potentials contributing to this model are identified using SExtractor with their parameters being optimized by the Bayesian Markov chain Monte Carlo (MCMC) sampler used in LENSTOOL. For each image (F160W, F105W,  $K_s$ , SMA) the whole arc is broken down into four ellipses of varying size and brightness which are created using measured elliptical sizes and flux densities from SExtractor. These ellipses are then passed through the LENSTOOL model to reconstruct the source plane image.

Figure 2 shows Keck/NIRC2  $K_s$ -band image, with the gravitational potentials used in the model circled in green, and the critical and caustic lines overlaid. From Gladders & Yee (2005) the cluster members used in the model are at photometric  $z = 0.997 \pm 0.017$  based on  $r$  and  $z$  band imaging. We assume a constant mass-to-light ratio and use a standard  $0.5''$  uncertainty, for strong lensing, in the position of the critical lines. The lens galaxies are modeled using a pseudo-elliptical isothermal

mass density profile (PIEMD) (Kneib et al. 1996). To create the model the other sources in the field of unknown redshift were also placed at  $z = 0.997$ . There are a total of 26 galaxies used in the model, most of which are out of view in the figure and do not contribute significantly to the modeled potential. The cluster members which contribute the largest potential to the model are the galaxies which fall in the blue critical lines in the figure. The cluster component to the east of the lensing arc has an average velocity dispersion of  $\sim 250$  km s $^{-1}$  while the west cluster component has an average velocity dispersion of  $\sim 230$  km s $^{-1}$ .

The counter-image from the lens model can be seen in the middle panel of Figure 4. The residual image in Figure 4 corresponds to the foreground cluster members being removed from the imaging using GALFIT (Peng et al. 2002), there is a small excess of flux in the region which should contain a counter-image but it falls within  $1 \sigma$  of the background noise. This may be due to an imperfect subtraction in the GALFIT modeling of the galaxies. In the model image the counter image is detected at  $\sim 5 \sigma$  above the background noise. The intensity of the counter-image is small compared to the overlapping cluster members which makes identifying the counter-image difficult. While the model is not unique it is well enough constrained that the results would not change significantly.

Models with multiply-imaged systems resulted in lenses that were too large and unrealistic. Therefore, a model assuming a singly imaged source was utilized. As a main constraint, we assumed that the central thin part of the arc was overlapping the critical line, as has been observed for some very elongated arcs (see the Clone arc in Jones et al. 2010). Placing the critical line closer to the arc results in increased stretching. The arc of HATLAS J132427 is very stretched, thus the critical line must overlap with the arc. However, the critical line cannot cross the arc, otherwise there would be two images. This approach results in a better constrained, singly imaged and elongated arc.

Figure 5 shows the imaging for four bands F105W, F160W,  $K_s$  and SMA along with their model in the image plane, the residual and the source plane reconstruction. The long arc is detected in the near-IR bands, with the SMA flux not contributing to the arc in a significant way. The SMA portion might be underestimated as the short baseline lengths are such that recovering a structure of  $15''$  might not be possible. The lens model produces an arc for the SMA contribution which would be undetected in the observed SMA flux. The stellar portion of HATLAS J132427 corresponds to the large extended arc suggesting it has a higher magnification than the dust portion. The best fit model gives  $\mu_{\text{dust}} = 4.9 \pm 1.8$  while the stellar magnification making up the extended arc is  $\mu_{\text{stars}} = 15.7 \pm 4.3$ . In George et al. (2013) a magnification estimate for the molecular gas is derived following Harris et al. (2012) and Bothwell et al. (2013). Using the  $J=1 \rightarrow 0$  luminosity and the FWHM,  $\mu_{\text{Gas}}$  is found to be  $\sim 11$ . Due to the large uncertainty in the FWHM of the gas (e.g.  $640 \pm 270$  km s $^{-1}$ ) the final estimate of the error for the derived value is  $\pm 7$  which is consistent with the magnification values found with the lens model used here. In Bussmann et al. (2013) a lens model for SMA using two galaxies instead of the two cluster components

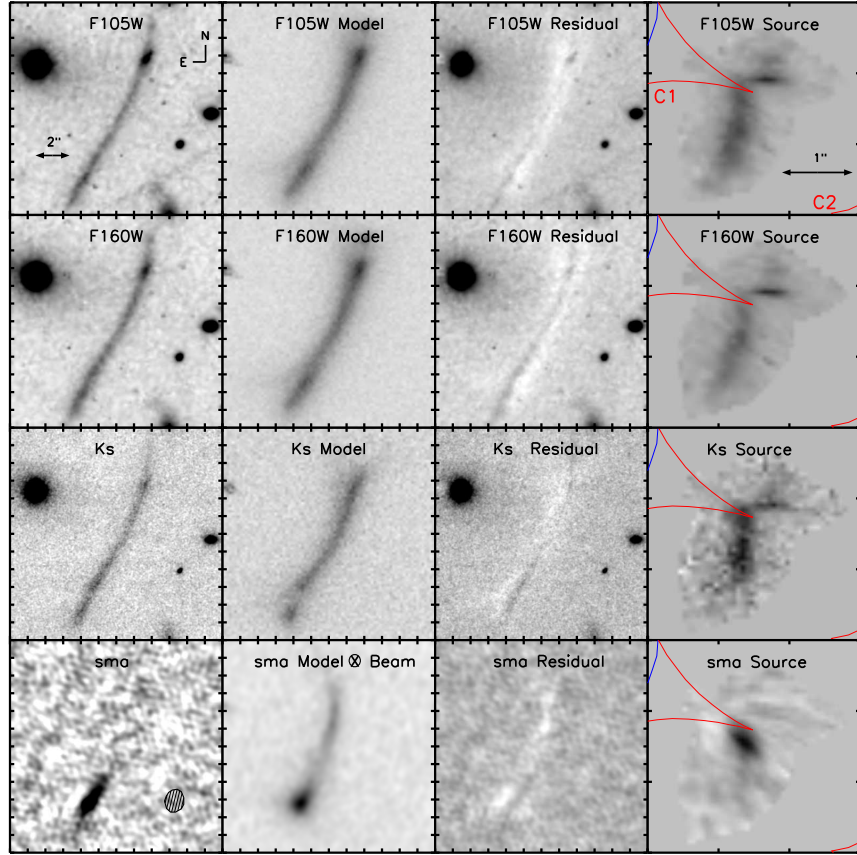


**Figure 5.** Lens modeling of HATLAS J132427 at several optical/infrared wavelengths and at  $870\ \mu\text{m}$ . *1st column:* The original imaging for the two HST bands, as well as Keck and SMA. The beam size and orientation is overlaid on the SMA frame. *2nd column:* Image obtained with the lens model for each band. The SMA model is convolved with a 2D Gaussian model of the SMA beam. *3rd column:* The residual obtained by subtracting the model from the original image. The scale is set to see the areas of over and under subtraction. *4th column:* The source plane reconstruction for each band, with the critical and caustic lines overlaid in blue and red, respectively. The C1 and C2 refer to the caustic lines as shown in Figure 2.

resulted in a magnification of  $2.8 \pm 0.4$ . The SMA data having just one image in Bussmann et al. (2013) made the model more difficult to constrain whereas the multi-wavelength model presented here includes SMA, Keck, HST etc. and can be considered a more complete model of the dust magnification.

The third column of Figure 5 shows the residual when subtracting the model from the image. It is clear in the residual images that the models are more extended than the images leading to an over subtraction on the edges of the residual. There is a thin feature running down the middle of the residual image which suggests an under subtraction due to the original image being more peaked in the middle compared to the model. The image plane models were created in LENSTOOL using the source plane reconstructions with added Poisson noise and are a pixel to pixel reconstruction of the source plane image based on brightness intensity passed back through the same gravitational potential. The relative size and brightness of the model image compared to the original image could be a result of the magnification factors being underestimated.

## 5. SPECTRAL ENERGY DISTRIBUTION MODELING

The spectral energy distribution (SED) of HATLAS J132427 was analyzed using the Multi-wavelength Analysis of Galaxy Physical Properties (MAGPHYS) soft-

ware (da Cunha et al. 2008). The MAGPHYS package compares the observed flux density values to a library of model SEDs at the same redshift. Here we use the new HIGHZ model library of MAGPHYS SEDs, which was developed to interpret observations of SMGs from the ALESS survey (da Cunha et al. 2015), and should be more appropriate to fit the SEDs of DSFGs at high redshift.

The photometry for CHFT, HST and Keck were done using the SExtractor package (Bertin & Arnouts 1996) using a flexible elliptical aperture to account for the elongated nature of the source. The WISE photometry comes from the online WISE catalogs. The remaining photometry comes from George et al. (2013) and is discussed in Section 3. Table 2 lists the observed photometry used in the model fit with a spectroscopic redshift of 1.68. Because there is differential magnification for the dust and stellar components (Calanog et al. 2014) the observed fluxes were demagnified based on wavelength. The stellar fluxes corresponding to the full arc in the SED were demagnified by  $15.7 \pm 4.3$  while the dust portion centered on the lower bright clump was demagnified by  $4.9 \pm 1.8$ .

The spatial inhomogeneity of a background galaxy at different wavelengths can become more pronounced due to the effect of gravitational lensing (see Fu et al. 2012; Calanog et al. 2014). This differential magnifica-

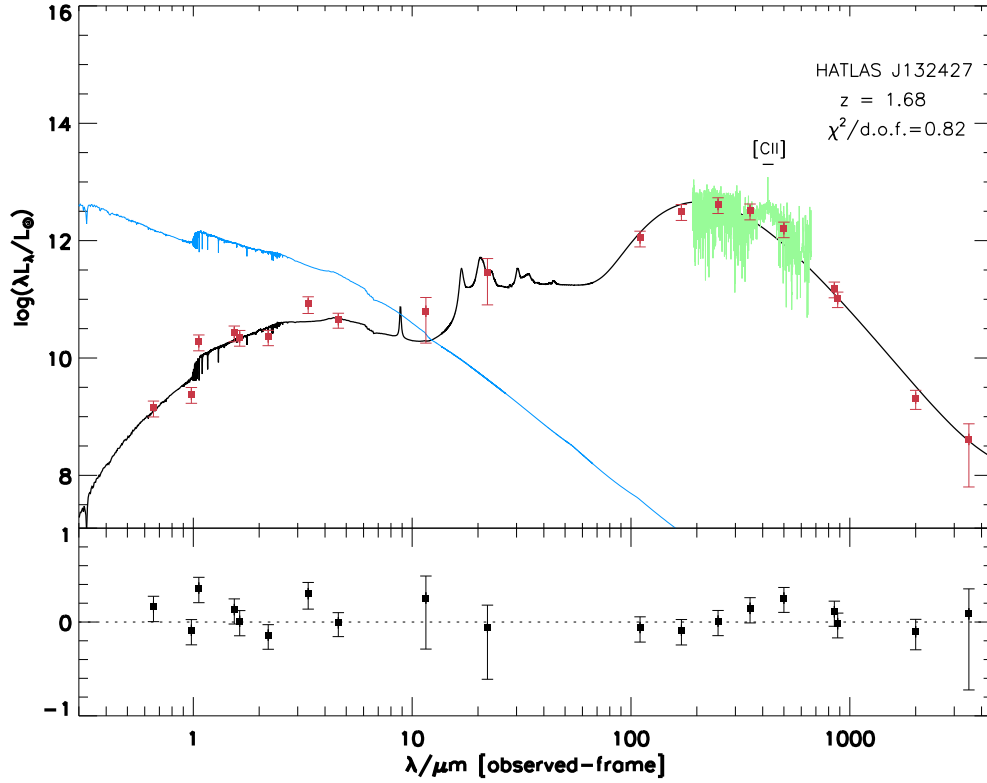


**Figure 6.** Top: The best-fit SED model is plotted in black while the intrinsic model without dust extinction is plotted in blue. The flux values have been demagnified based on wavelength. The *Herschel* FTS spectrum is shown in green. The FTS spectrum is not used in the SED fit but is shown here for reference. Bottom: The residuals for each fit.

tion leads to magnification values that are wavelength dependent. When doing a spectral energy distribution analysis, the observed fluxes need to be demagnified by the corresponding magnification value in order to find the intrinsic physical properties. Thus it is crucial when doing an SED analysis on a lensed galaxy to do a multi-wavelength lens model in order to derive the wavelength dependent magnification values.

The WISE W3 and W4 bands, at 12 and 22  $\mu\text{m}$  respectively, posed a problem as the MAGPHYS model SED showed those flux densities were a combination of both stellar and dust emission. In order to account for the uncertainty the error bars were extended to cover the entire magnification range, with flux densities corrected by 10, corresponding to the average of the dust and stellar magnification factors. Several fits were performed using a lower magnification for the W4 band, corresponding to more dust emission, as well as a higher magnification for the W3 band, corresponding to higher stellar contribution, in the end the average value provided the best fit.

We note that the SMA and IRAM PdBI flux measurements might be underestimated in the fit due to the short baseline coverage of the SMA and PdBI observations. This could lead to an underestimate of the SFR which is correlated with the total dust luminosity (Kennicutt 1998). The dust temperature is also correlated with the dust luminosity (Chapman et al. 2005) and therefore could also be underestimated.

Figure 6 shows the final best fit for the SED plotted in

black while the intrinsic model without dust extinction is plotted in blue. The physical properties derived from the SED fit are listed in Table 3. The FTS spectrum, with the [CII] line labeled, is shown for reference and not used in the fit. The  $\chi^2$  per degree of freedom is 0.82.

## 6. DISCUSSION

Our knowledge of the physical properties of DSFGs remains limited and the goal of recent studies is to increase our understanding of the starburst phenomena in DSFGs. For this purpose we examine the various components of the galaxy, including the dust temperature, the ratio of gas to baryons, the star formation rate and its density as well as the far-infrared radio correlation. We start with a discussion of the physical properties derived from the SED fit and compare them to other SMGs and DSFGs.

From the SED analysis the estimated dust temperature is  $\sim 30$  K which is low when compared with other SMGs (Amblard et al. 2010), and would signify a lack of significant AGN heating. In Figure 7 we examine the effect of gravitational lensing on the ratio of dust temperature to FIR luminosity. From Greve et al. (2012) the high FIR luminosity to dust temperature ratio is suggestive of a high magnification factor. In DSFGs an increased FIR luminosity correlates to an increased dust temperature. Both values come from the SED fit and are in agreement with the other high- $z$  strongly lensed galaxies although as mentioned in Section 5 they might be underestimated which could account for the source being on the edge of the grouping of strongly lensed galaxies. For



**Table 2**  
Photometry of HATLAS J132427

Instrument	$\lambda$	$S_\nu$
CHFT (r band)	0.66 $\mu\text{m}$	$0.05 \pm 0.01 \mu\text{Jy}$
CHFT (z band)	0.98 $\mu\text{m}$	$0.09 \pm 0.01 \mu\text{Jy}$
HST (F105W)	1.06 $\mu\text{m}$	$0.79 \pm 0.4 \mu\text{Jy}$
HST (F160W)	1.54 $\mu\text{m}$	$1.81 \pm 0.6 \mu\text{Jy}$
Keck (H band)	1.63 $\mu\text{m}$	$2.41 \pm 0.8 \mu\text{Jy}$
Keck (Ks band)	2.20 $\mu\text{m}$	$3.92 \pm 0.6 \mu\text{Jy}$
WISE W1	3.35 $\mu\text{m}$	$0.30 \pm 0.01 \text{ mJy}$
WISE W2	4.60 $\mu\text{m}$	$0.22 \pm 0.01 \text{ mJy}$
WISE W3	11.56 $\mu\text{m}$	$0.32 \pm 0.03 \text{ mJy}$
WISE W4	22.09 $\mu\text{m}$	$2.81 \pm 0.7 \text{ mJy}$
<i>Herschel</i> (PACS)	100 $\mu\text{m}$	$41 \pm 4 \text{ mJy}$
<i>Herschel</i> (PACS)	160 $\mu\text{m}$	$180 \pm 14 \text{ mJy}$
<i>Herschel</i> (SPIRE)	250 $\mu\text{m}$	$347 \pm 25 \text{ mJy}$
<i>Herschel</i> (SPIRE)	350 $\mu\text{m}$	$378 \pm 28 \text{ mJy}$
<i>Herschel</i> (SPIRE)	500 $\mu\text{m}$	$268 \pm 21 \text{ mJy}$
SCUBA2 JCMT	850 $\mu\text{m}$	$43 \pm 1.2 \text{ mJy}$
SMA	870 $\mu\text{m}$	$30.2 \pm 5.2 \text{ mJy}$
PdBI	2 mm	$1.2 \pm 0.1 \text{ mJy}$
CARMA	3.5 mm	$200 \pm 170 \mu\text{Jy}$
VLA	4.3 cm	$350 \pm 30 \mu\text{Jy}$
VLA	21 cm	$1.95 \pm 0.24 \text{ mJy}$

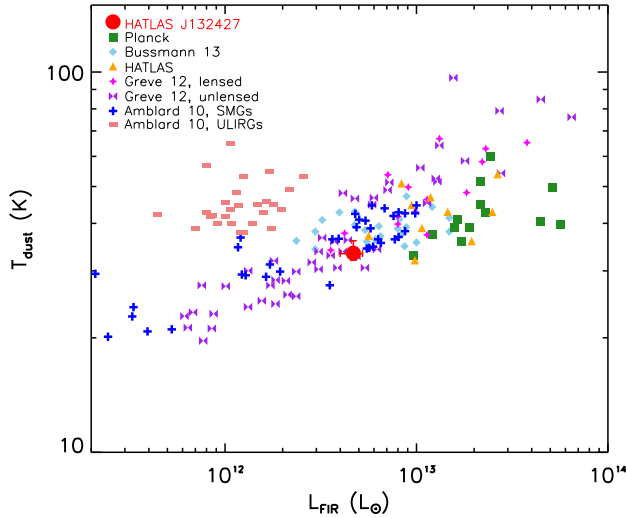


**Figure 7.** Dust temperature vs. FIR luminosity. For comparison other lensed and non lensed galaxies are plotted, including the other Planck/*Herschel* detected lensed galaxies (Canameras et al. 2015), *Herschel* lensed galaxies (Bussmann et al. 2013) as well as other lensed/unlensed SMGs and ULIRGs (Greve et al. 2012; Amblard et al. 2010). To make the comparison more instructive the lensed galaxies have had  $L_{\text{FIR}}$  demagnified by a factor of 5.

the purposes of this discussion the differential magnification has been divided into stellar and dust components. It is possible that there could be differential magnification between warm and cool dust emission which would lead to less confidence in the dust temperature estimate. Greve et al. (2012) estimates the magnification factor for the lensed galaxies to be a factor of 1-10 which is consistent with the magnification factor ( $\mu_{\text{dust}} \sim 5$ ) from the

**Table 3**  
SED fit and derived properties

SED fit	
$f_\mu(\text{SFH/IR})$	$0.857^{+0.20}_{-0.35}$
$A_V$	$4.19^{+0.20}_{-0.24}$
$M_*$	$11.2^{+3.2}_{-3.8} 10^{10} M_\odot$
SFR	$390^{+60}_{-57} M_\odot \text{yr}^{-1}$
$L_{\text{dust}}$	$46.8^{+5.6}_{-7.0} 10^{11} L_\odot$
$M_{\text{dust}}$	$13.9^{+3.0}_{-2.8} 10^8 M_\odot$
$T_{\text{dust}}$	$33.9^{+2.1}_{-1.9} \text{ K}$
sSFR	$30 \pm 2 10^{-10} \text{yr}^{-1}$
Derived Properties	
$\alpha_{\text{CO}}^1$	$1.02 \pm 0.13$
	$M_\odot (\text{K km s}^{-1} \text{pc}^2)^{-1}$
$\mu_{\text{dust}}$	$4.9 \pm 1.8$
$\mu_{\text{stars}}$	$16 \pm 4.3$
$r_{\text{eff Gas}}$	$\sim 9 \text{ kpc}$
$r_{\text{eff Dust}}$	$\sim 2 \text{ kpc}$
$\Sigma_{\text{SFR}}$	$32.9^{+13.1}_{-13.0} M_\odot \text{yr}^{-1} \text{kpc}^{-2}$
$\Sigma_{\text{gas}}$	$323 \pm 132 M_\odot \text{pc}^{-2}$
$M_{\text{gas}}$	$8.6 \pm 3.2 \times 10^{10} M_\odot$
Gas Fraction ( $M_{\text{gas}}/(M_{\text{star}}+M_{\text{gas}})$ )	$0.44 \pm 0.14$

<sup>1</sup> Based on Narayanan et al. (2012)

lens model for HATLAS J132427.

In order to estimate the molecular gas mass, we need the conversion factor between CO and  $\text{H}_2$ , commonly known as  $\alpha_{\text{CO}}$  in the literature (Carilli & Walter 2013). Here, we make use of results from numerical simulations by Narayanan et al. (2012) where  $\alpha_{\text{CO}} = 10.7 \times W_{\text{CO}}^{-0.32} \times Z^{-0.65}$ , when  $W_{\text{CO}}$  is the CO surface brightness and  $Z$  is metallicity. We refer the reader to Solomon & Vanden Bout (2005) equation 3 for the  $L'_{\text{CO}}$  calculation and  $W_{\text{CO}}$  is obtained as  $L'_{\text{CO}}/\text{area}$  observed. For this estimate we make use of the area observed based on the resolved CO2-1 image from CARMA which results in a dust area of  $\sim 10 \text{ kpc}^2$ . We assume solar metallicity for the fit, which is consistent with other SMGs (Erb et al. 2006). The numerical simulation-calibrated relation results in an  $\alpha_{\text{CO}}$  of  $1.02 \pm 0.13 M_\odot (\text{K km s}^{-1} \text{pc}^2)^{-1}$ , which is in agreement with the literature for SMGs. Tacconi et al. (2008) as well as Hodge et al. (2012) find  $\alpha_{\text{CO}} \sim 1$ . Using this value for the CO- $\text{H}_2$  conversion factor the gas mass is derived and found to be  $8.6 \pm 3.2 \times 10^{10} M_\odot$ . We assume the magnification factor of the gas distribution to be  $\mu = 4.9$ , consistent with the dust. An alternative calculation for the gas mass



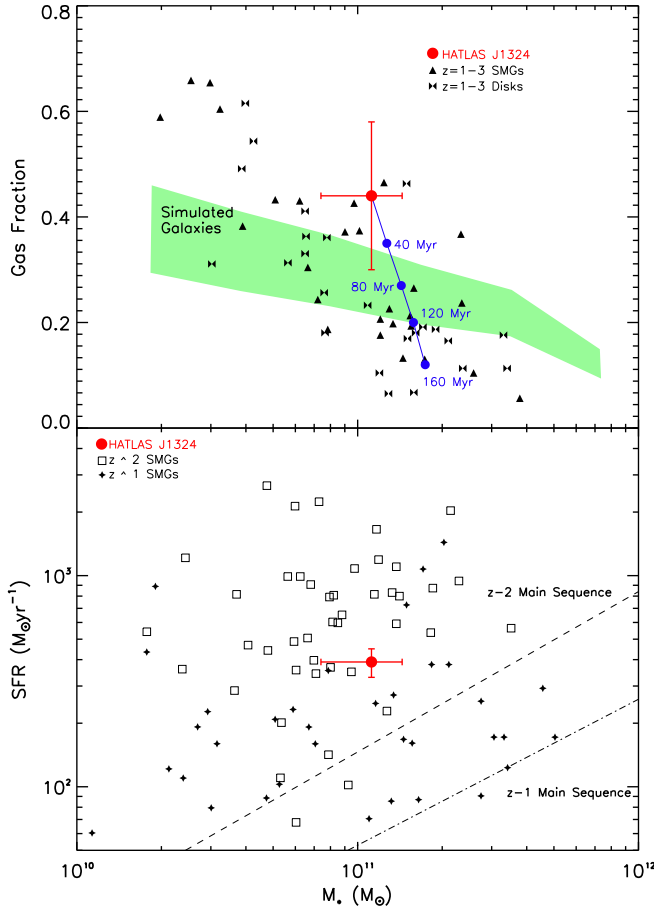


**Figure 8.** Top: Gas fraction vs. stellar mass. The other objects are from Narayanan et al. (2012). The green shaded region represents star forming galaxies at  $z = 2$  from cosmological hydrodynamic simulations (Davé et al. 2010). The blue circles represent the evolution of HATLAS J132427 over the course of 160 Myr. Each successive circle represents an 40 Myr time step with a constant SFR and mass conservation. Bottom: Star formation rate vs. stellar mass. For comparison  $z \sim 2$  SMGs are plotted (Fu et al. 2013) as well as  $z \sim 1$  SMGs (Michałowski et al. 2010; Tacconi et al. 2010b; Banerji et al. 2011; Timmons et al. 2015). The  $z = 1$  and  $z = 2$  main sequence (Ma et al. 2015) are also plotted.

comes from Scoville et al. (2014), using the ratio of the gas mass to the  $850 \mu\text{m}$  luminosity giving an estimated gas mass to be  $6.1 \pm 3.1 \times 10^{10} M_\odot$  which is consistent with the gas mass estimated from  $\alpha_{\text{CO}}$  derived above.

The top portion of Figure 8 shows the gas-to-baryon fraction vs. stellar mass. For comparison  $z = 1-3$  SMGs are plotted as well as  $z = 1-3$  main sequence star forming galaxies. For its stellar mass, HATLAS J132427 has a large gas-to-baryon ratio ( $M_{\text{gas}}/(M_{\text{star}}+M_{\text{gas}})$ ) of 0.44. This is in agreement with other measurements of high- $z$  star forming galaxies (Tacconi et al. 2013). The green shaded region in Figure 8 shows star forming galaxies at  $z = 2$  from cosmological hydrodynamic simulations (Davé et al. 2010). In Narayanan et al. (2012) it is suggested that  $\alpha_{\text{CO}}$  is overestimated for systems at high redshift which could account for some of the scatter. The blue circles on Figure 8 represent the future evolution of HATLAS J132427 assuming a constant SFR and mass conservation. Each blue dot represents a time step 40

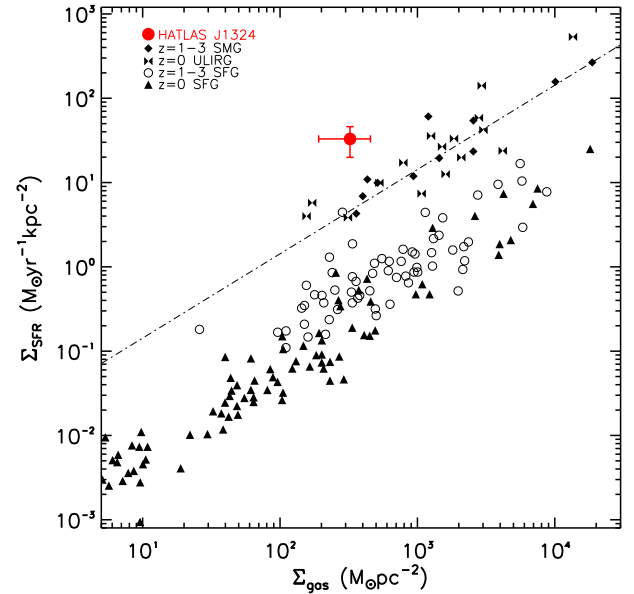


**Figure 9.** Star-formation-rate surface density vs. molecular gas surface density for local ULIRGs and SFGs as well as  $z \sim 1-3$  SMGs and SFGs. For comparison SFGs are plotted (Kennicutt 1998), as well as SMGs and local ULIRGs (Tacconi et al. 2013; Fu et al. 2013). The dashed line represents a constant gas consumption ( $\tau_{\text{disk}} = \Sigma_{\text{gas}}/\Sigma_{\text{SFR}}$ ) of 70 Myr for star forming disks.

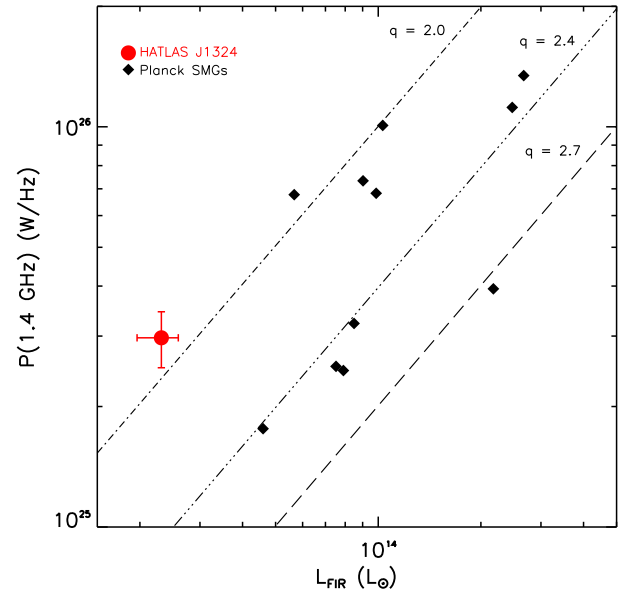


**Figure 10.** The far-infrared radio correlation for Planck and *Herschel* detected lensed DSFGs. The other Planck detected galaxies are from Canameras et al. (2015) and represent the total number of high-redshift lensed galaxies detected in both Planck and *Herschel*. The lines represent varying  $q$  values ( $\log L_{\text{FIR}}/(3.75 \times 10^{12} \text{ W}) - \log L_{1.4}/(\text{W Hz}^{-1})$ ) of 2.0, 2.4, and 2.7.

Myr and shows the slope of the evolution as being steeper than the overall trend of gas fraction vs.  $M_*$ , due to the fact that some gas must be recycled.

The bottom portion of Figure 8 shows the star formation rate vs. stellar mass. Also plotted are  $z \sim 1$  SMGs and  $z \sim 2$  SMGs from the literature for comparison. HATLAS J132427 is above the main sequence lines for both  $z=1$  (Elbaz et al. 2007) and  $z=2$  (Daddi et al. 2007). This is consistent with the large gas mass of HATLAS J132427 and its being observed in a star bursting phase.

Figure 9 shows the star formation surface density vs. molecular surface density. Plotted for comparison are  $z = 1 - 3$  SMGs and SFGs, as well as local ULIRGs and SFGs. The gas area and effective gas radius is calculated using the observed gas area from CARMA and computing a demagnified gas area based on the lens model. The dust area and effective dust radius are calculated by measuring the area of the SMA source plane reconstruction. The dust area is likely underestimated due to the fact that the SMA beam size restricts the flux area of the SMA map. The resulting SMA source plane reconstruction is likely larger than the measured area. This could account for the source having a higher star formation density than the similar SMGs and ULIRGs. The gas consumption time  $\tau_{\text{disk}}$ , which refers to the star forming disk region can be calculated using the ratio  $\tau_{\text{disk}} = \Sigma_{\text{gas}}/\Sigma_{\text{SFR}}$ . For HATLAS J132427 the gas consumption time is  $\sim 10$  Myr. The dot dashed line on the plot represents  $\tau_{\text{disk}} = 70$  Myr, which is populated with SMGs and ULIRGs while the more quiescent star forming galaxies have  $\tau_{\text{disk}} \sim 1.5$  Gyr. This short timescale of star formation for HATLAS J132427 is consistent with other DSFGs.

We investigate the possibility of an AGN contribution to this source by examining the correlation between FIR and 1.4 GHz radio luminosity which is shown in Figure 10. It is common to define this correlation in terms of a value  $q$  which is defined as  $q = \log L_{\text{IR}}/(3.75 \times 10^{12} \text{ W}) - \log L_{1.4}/(\text{W Hz}^{-1})$ . A spectral index  $\alpha = -0.8$  is assumed (Condon 1992). The  $q$  value for HATLAS J132427 is 1.90 which is lower than the average for DSFGs  $\sim 2.4$  (Ivison et al. 2010). The low  $q$  value corresponds to a high relative luminosity in the radio emission and might suggest that HATLAS J132427 has a luminous AGN (e.g., Vlahakis et al. 2007; Bourne et al. 2011). It is assumed in this calculation that the radio and FIR luminosity are being magnified by the same factor. The output values of MAGPHYS are not strongly affected by AGN contamination (da Cunha et al. 2015). Hayward & Smith (2015) shows that strong AGN contamination can lead to an overestimation of the stellar mass in a SED analysis. If the longer wavelength radio is less magnified due to differential lensing the  $q$  value would be underestimated as a result. As mentioned in Section 5 the dust luminosity might be underestimated and the  $q$  value would as a result also be underestimated.

## 7. SUMMARY

HATLAS J132427.0+284452 is a *Herschel* Astrophysical Terahertz Large Area Survey (H-ATLAS) selected strongly lensed arc of length  $\sim 15''$  at  $z = 1.68$ . HATLAS J132427 is also Planck detected at  $1.30 \pm 0.15$  Jy in the 350  $\mu\text{m}$  band and is one of a few high- $z$  Planck

detections in H-ATLAS. A lens model with source plane reconstructions at several wavelengths allows the estimation of magnification factors for the stars  $\mu_{\text{stars}} \sim 16$  and the dust  $\mu_{\text{dust}} \sim 5$ . The different magnification values for the dust and stellar components become important for the SED analysis in which the observed fluxes must be demagnified according to wavelength. This source demonstrates the fact that lens models constructed in a single wavelength should not be considered complete due to the effect of differential lensing.

Physical properties of the galaxy are estimated by fitting model SEDs gives a SFR of  $\sim 400 \text{ M}_{\odot}\text{yr}^{-1}$  and a stellar mass of  $\sim 11 \times 10^{10} \text{ M}_{\odot}$  which are consistent with a high- $z$  dusty star forming galaxy. The SFR surface density  $30 \text{ M}_{\odot}\text{yr}^{-1}\text{kpc}^{-2}$  is high compared to the molecular gas surface density  $300 \text{ M}_{\odot}\text{pc}^{-2}$ . This comes from the lens model reconstruction of the dust area which reveals a large amount of star formation is happening in a single clump. There is some reason to believe that the dust area is underestimated due to the beam size used in the SMA observations used to model the dust area. We find that the gas fraction is slightly higher than star forming galaxies from cosmological hydrodynamic simulations but still consistent with other observations of SMGs at this redshift. The far-infrared radio correlation suggests that HATLAS J132427 might host a luminous AGN or it might be an artifact of differential lensing.

Financial support for this work was provided by NASA through grant HST-GO-13399 from the Space Telescope Science Institute, which is operated by Associated Universities for Research in Astronomy, Inc., under NASA contract NAS 5-26555. Additional support for NT, AC and HN was from NSF through AST-1313319. Some of the data presented herein were obtained at the W.M. Keck Observatory, which is operated as a scientific partnership among the California Institute of Technology, the University of California and the National Aeronautics and Space Administration. The Observatory was made possible by the generous financial support of the W.M. Keck Foundation. The authors wish to recognize and acknowledge the very significant cultural role and reverence that the summit of Mauna Kea has always had within the indigenous Hawaiian community. We are most fortunate to have the opportunity to conduct observations from this mountain. The Submillimeter Array is a joint project between the Smithsonian Astrophysical Observatory and the Academia Sinica Institute of Astronomy and Astrophysics and is funded by the Smithsonian Institution and the Academia Sinica. C. Furlanetto acknowledges funding from CAPES (proc. 12203-1). J.G.N. acknowledges financial support from the Spanish MINECO for a Ramon y Cajal fellowship. I.O. acknowledges support from the European Research Council in the form of the Advanced Investigator Programme, 321302, COSMICISM.

## REFERENCES

- Amblard, A., Cooray, A., Serra, P., et al. 2010, A&A, 518, L9
- Banerji, M., Chapman, S. C., Smail, I., et al. 2011, MNRAS, 418, 1071
- Bertin, E., & Arnouts, S. 1996, A&AS, 117, 393

- Bothwell, M. S., Smail, I., Chapman, S. C., et al. 2013, *MNRAS*, 429, 3047
- Bourne, N., Dunne, L., Ivison, R. J., et al. 2011, *MNRAS*, 410, 1155
- Bussmann, R. S., Pérez-Fournon, I., Amber, S., et al. 2013, *ApJ*, 779, 25
- Calanog, J. A., Fu, H., Cooray, A., et al. 2014, *ApJ*, 797, 138
- Canameras, R., Nesvadba, N. P. H., Guery, D., et al. 2015, *ArXiv e-prints*, arXiv:1506.01962
- Carilli, C. L., & Walter, F. 2013, *ARA&A*, 51, 105
- Casey, C. M., Narayanan, D., & Cooray, A. 2014, *Phys. Rep.*, 541, 45
- Chapman, S. C., Blain, A. W., Smail, I., & Ivison, R. J. 2005, *ApJ*, 622, 772
- Condon, J. J. 1992, *ARA&A*, 30, 575
- da Cunha, E., Charlot, S., & Elbaz, D. 2008, *MNRAS*, 388, 1595
- da Cunha, E., Walter, F., Smail, I. R., et al. 2015, *ApJ*, 806, 110
- Daddi, E., Dickinson, M., Morrison, G., et al. 2007, *ApJ*, 670, 156
- Davé, R., Finlator, K., Oppenheimer, B. D., et al. 2010, *MNRAS*, 404, 1355
- Eales, S., Dunne, L., Clements, D., et al. 2010, *PASP*, 122, 499
- Elbaz, D., Daddi, E., Le Borgne, D., et al. 2007, *A&A*, 468, 33
- Erb, D. K., Shapley, A. E., Pettini, M., et al. 2006, *ApJ*, 644, 813
- Fu, H., Jullo, E., Cooray, A., et al. 2012, *ApJ*, 753, 134
- Fu, H., Cooray, A., Feruglio, C., et al. 2013, *Nature*, 498, 338
- Genzel, R., Tacconi, L. J., Gracia-Carpio, J., et al. 2010, *MNRAS*, 407, 2091
- George, R. D., Ivison, R. J., Hopwood, R., et al. 2013, *MNRAS*, 436, L99
- Gladders, M. D., Hoekstra, H., Yee, H. K. C., Hall, P. B., & Barrientos, L. F. 2003, *ApJ*, 593, 48
- Gladders, M. D., & Yee, H. K. C. 2005, *ApJS*, 157, 1
- González-Nuevo, J., Lapi, A., Fleuren, S., et al. 2012, *ApJ*, 749, 65
- Greve, T. R., Vieira, J. D., Weiß, A., et al. 2012, *ApJ*, 756, 101
- Griffin, M. J., Abergel, A., Abreu, A., et al. 2010, *A&A*, 518, L3
- Gruppioni, C., Pozzi, F., Rodighiero, G., et al. 2013, *MNRAS*, 432, 23
- Harris, A. I., Baker, A. J., Frayer, D. T., et al. 2012, *ApJ*, 752, 152
- Hayward, C. C., & Smith, D. J. B. 2015, *MNRAS*, 446, 1512
- Hodge, J. A., Carilli, C. L., Walter, F., et al. 2012, *ApJ*, 760, 11
- Holland, W. S., Bintley, D., Chapin, E. L., et al. 2013, *MNRAS*, 430, 2513
- Ivison, R. J., Smail, I., Barger, A. J., et al. 2000, *MNRAS*, 315, 209
- Ivison, R. J., Magnelli, B., Ibar, E., et al. 2010, *A&A*, 518, L31
- Jones, T., Ellis, R., Jullo, E., & Richard, J. 2010, *ApJ*, 725, L176
- Jullo, E., Kneib, J.-P., Limousin, M., et al. 2007, *New Journal of Physics*, 9, 447
- Kennicutt, Jr., R. C. 1998, *ARA&A*, 36, 189
- Kneib, J.-P., Ellis, R. S., Smail, I., Couch, W. J., & Sharples, R. M. 1996, *ApJ*, 471, 643
- Kümmel, M., Walsh, J. R., Pirzkal, N., Kuntschner, H., & Pasquali, A. 2009, *PASP*, 121, 59
- Lapi, A., González-Nuevo, J., Fan, L., et al. 2011, *ApJ*, 742, 24
- Lawrence, A., Warren, S. J., Almaini, O., et al. 2007, *MNRAS*, 379, 1599
- Le Floch, E., Papovich, C., Dole, H., et al. 2005, *ApJ*, 632, 169
- Lilly, S. J., Eales, S. A., Gear, W. K. P., et al. 1999, *ApJ*, 518, 641
- Ma, B., Cooray, A., Calanog, J. A., et al. 2015, *ApJ*, 814, 17
- Messias, H., Dye, S., Nagar, N., et al. 2014, *A&A*, 568, A92
- Michałowski, M., Hjorth, J., & Watson, D. 2010, *A&A*, 514, A67
- Narayanan, D., Bothwell, M., & Davé, R. 2012, *MNRAS*, 426, 1178
- Negrello, M., Perrotta, F., González-Nuevo, J., et al. 2007, *MNRAS*, 377, 1557
- Negrello, M., Hopwood, R., De Zotti, G., et al. 2010, *Science*, 330, 800
- Peng, C. Y., Ho, L. C., Impey, C. D., & Rix, H.-W. 2002, *AJ*, 124, 266
- Pilbratt, G. L., Riedinger, J. R., Passvogel, T., et al. 2010, *A&A*, 518, L1
- Planck Collaboration, Ade, P. A. R., Aghanim, N., et al. 2011, *A&A*, 536, A1
- Poglitsch, A., Waelkens, C., Geis, N., et al. 2010, *A&A*, 518, L2
- Scoville, N., Aussel, H., Sheth, K., et al. 2014, *ApJ*, 783, 84
- Solomon, P. M., & Vanden Bout, P. A. 2005, *ARA&A*, 43, 677
- Swinbank, A. M., Chapman, S. C., Smail, I., et al. 2006, *MNRAS*, 371, 465
- Tacconi, L. J., Genzel, R., Smail, I., et al. 2008, *ApJ*, 680, 246
- Tacconi, L. J., Genzel, R., Neri, R., et al. 2010a, *Nature*, 463, 781
- . 2010b, *Nature*, 463, 781
- Tacconi, L. J., Neri, R., Genzel, R., et al. 2013, *ApJ*, 768, 74
- Timmons, N., Cooray, A., Nayyeri, H., et al. 2015, *ApJ*, 805, 140
- Vlahakis, C., Eales, S., & Dunne, L. 2007, *MNRAS*, 379, 1042
- Wardlow, J. L., Cooray, A., De Bernardis, F., et al. 2013, *ApJ*, 762, 59
- Wizinowich, P. L., Le Mignant, D., Bouchez, A. H., et al. 2006, *PASP*, 118, 297